Research Square

Preprints are preliminary reports that have not undergone peer review.
They should not be considered conclusive, used to inform clinical practice,
or referenced by the media as validated information.

Experimental and analytical investigation on bond behavior between steel bars and steel fiber reinforced recycled aggregate concrete

Liping Kang
Zhengzhou University of Aeronautics
Ke Shi
shike@zua.edu.cn

Zhengzhou University of Aeronautics
Bo Pang
Zhengzhou University of Aeronautics
Haokun Wang
Zhengzhou University of Aeronautics

Article

Keywords: steel fiber reinforced recycled aggregate concrete, pullout test, bond behavior, SEM, finite element analysis

Posted Date: June 25th, 2026

DOI: https://doi.org/10.21203/rs.3.rs-9966769/v1

License: This work is licensed under a Creative Commons Attribution 4.0 International License.
Read Full License

Additional Declarations: No competing interests reported.

Version of Record: A version of this preprint was published at Scientific Reports on September 16th, 2026. See the published version at https://doi.org/10.1038/s41598-026-68913-9.

Experimental and analytical investigation on bond behavior between steel bars and steel fiber reinforced recycled aggregate concrete

Liping Kang, Ke Shi*, Bo Pang, Haokun Wang

School of Civil Engineering and Environment,Zhengzhou University of Aeronautics, 450015,China

* Corresponding author at: School of Civil Engineering and Environment, Zhengzhou University of Aeronautics, Zhengzhou 450015, Henan, China

Email addresses: shike@zua.edu.cn (Shi Ke)

ABSTRACT: In this study, the bond behavior between steel bars and steel fiber reinforced recycled aggregate concrete (SFRAC) was investigated by conducting 27 pullout tests. The main test parameters included the concrete strength grade, recycled coarse aggregate replacement ratio, steel fiber volume fraction, and anchorage length. Based on the test results, the failure mode, bond strength, and bond stress-slip curve of SFRAC bond specimens were analyzed. The results indicated that the ultimate and residual bond strength between the SFRAC and steel bars increases with an increase in the concrete strength grade and decreases with an increase in the recycled coarse aggregate replacement ratio and anchorage length. The addition of steel fiber can greatly improve the residual bond strength. However, the steel fiber volume fraction has little effect on the ultimate bond strength. Scanning electron microscopy was performed to characterize the bonding mechanism of the steel fiber on concrete and the microstructure of the interfacial transition zone of the SFRAC. Furthermore, an analytical model for simulating the bond-slip relationship was established by data fitting. Finally, finite element simulations were performed using ABAQUS software, and the results of the experiments and simulations were compared. The results showed that the proposed model has high accuracy and can be used to simulate the bond behavior between steel bars and SFRAC.

Keywords: steel fiber reinforced recycled aggregate concrete; pullout test; bond behavior; SEM; finite element analysis.

1. Introduction

Rapid urbanization and large-scale infrastructure construction have led to the depletion of natural sand and stone resources. In addition, the demolition of old buildings and infrastructure projects leads to the accumulation of large amounts of construction and demolition waste, which will pollute the environment [1]. It is widely recognized that recycled aggregate concrete (RAC) prepared by the

recycled aggregate (RA) is an effective strategy to consume concrete waste as well as conserve the natural resources and solve the environmental pollution [2,3]. However, compared to natural aggregate concrete (NAC), RAC has inferior compressive strength [4], tensile strength [5], durability [6] and bonding performance [7,8] due to its inherent defects of RA, such as lower strength, higher water absorption, and higher porosity [9]. These limit the application of RAC in structural elements [10,11]. In order to mitigate the defects of RAC and expand the scope of its application, global researchers have proposed several feasible methods. The addition of steel fiber (SF) is recognized as an available and convenient solution to improve mechanical and ductility of RAC as well as enhance interfacial concrete-steel bond [12,13,14].

The bond performance between steel reinforcement and concrete is the key factor for the two materials to work together in steel-concrete structures. Numerous studies have extensively investigated the bond behavior between steel bars and RAC[15,16,17,18,19]. Kim et al. [20] evaluated the effect of RCA on the deformed steel-to-concrete bond strength and concluded that the bond strength of deformed steel rebars embedded in RAC decreased as the compressive strength of RCA increased. Leibovich and Yankelevsky [21] also pointed out that the maximum bond stress is not affected by the aggregate type but in accordance with the concrete compressive strength. However, some studies [15,22,23,24]showed that the bond behavior between steel rebars and RAC was similar or superior to that for normal concrete and steel rebars. In a word, the bond-slip law between steel bars and RAC is quite different from that of steel bars with NAC. As a reinforcement material, steel fibers can effectively restrain the crack formation, development and growth [25,26]. Besides, the interfacial bond properties of steel with steel fiber reinforced recycled aggregation concrete (SFRAC) will be improved due to the fiber bridging-effect [27]. Hence, the bond-slip constitutive model of steel bars with SFRAC is different from that of steel with RAC. The influence of steel fibers on the bond behavior between steel rebar and RAC and the bond-slip relationship is significant.

In order to promote the application of SFRAC in practical engineering structures, it is necessary to have a detailed understanding about the fundamental mechanical properties and the bonding behavior of steel bars with SFRAC. To date, many scholars have investigated the mechanical and durability performance of steel fiber reinforced recycled aggregate concrete in terms of compressive strength

[28,29,30], tensile strength [31], flexural strength [32,33], water and chloride permeability [34,35,36] and so on. Meanwhile, the strength, deformation and failure models of SFRAC under multi-axial loading conditions were successively proposed [37,38,39]. Researches demonstrated that SFRAC was very suitable as a structural material due to its excellent mechanical performance and some studies about the behavior of SFRAC elements had been revealed [40,41,42]. However, relatively few studies have been conducted on the bond between steel bars and SFRAC. He et al [43] studied the bond-slip performance of steel bars in steel-fiber high-strength recycled concrete and established a constitutive model based on the test results. It proposed that the replacement ratio of RCA should not be higher than 30% and the addition ratio of steel fiber should not exceed 0.8%. While the bond-slip relationship and conclusions are reasonable for high-strength steel-fiber recycled concrete, further researches are needed on whether the bonding property of steel rebars embedded in normal-strength SFRAC is applicable. Gao et al [44] revealed the bond behavior between steel bars and steel-polypropylene hybrid fiber reinforced recycled aggregate concrete. It proposed that the steel fibers played a greater role in the bond strength and the development of cracks compared to polypropylene fibers. In addition to being detrimental to work performance, the bond-slip constitutive relationship is also unsuitable for hybrid fiber. The satisfactory use of SFRAC depends on the bond behavior between steel bars and SFRAC. Therefore, it is necessary and urgent to investigate the bond mechanisms and the development of bond-slip constitutive model between the steel bars and SFRAC, which will promote the application and development of steel rebar-reinforced SFRAC structures.

Given this context, this paper presents a systematic study on the bond behavior between steel bars and SFRAC through pullout tests. Based on the experimental results, the failure model, bond strength, and bond stress-slip curve of SFRAC bond specimens were analyzed. A new bond stress–slip constitutive model that could accurately simulate the entire bond behavior was derived. In addition, to solve the problems of low accuracy and efficiency when considering the bond behavior of SFRAC structures in finite element analysis (FEA), a practical and accurate method for considering the bond behavior in the finite element model was proposed. The comparison between the numerical and experimental results shows that the bond behavior between the steel bars and SFRAC can be accurately simulated using the proposed FEA method.

2. Experimental program

2.1. Materials and mixture proportions

According to Chinese Standard GB175-2007 (2007)[45], Ordinary Portland Cement (P.O.42.5) with a surface area of 355 m^2/kg was used. The coarse aggregates employed including natural coarse aggregate (NCA) (Fig. 1(a)) and recycled concrete aggregate (RCA) (Fig. 1(b)). RCA was obtained by crushing, sieving and cleaning from scientific research waste beams after removing the steel bars. The NCA and RCA was continuously graded crushed stone with particle sizes of 5-25mm. In addition to being similar, the grading curves of the two types of coarse aggregates were also within the coarse aggregate grading limit specified by Chinese standard GB25177-2010 (2010)[46]. The fine aggregate was natural river sand with a fineness modulus of 2.75. As shown in Fig. 1(c), the length-diameter ratio of hooked-end steel fiber used was 64, and the nominal yield tensile strength was 1345 MPa. According to Chinese Standard GB8076-2008 (2008), 1% polycarboxylate superplasticizer (PS) with a water-reducing agent was incorporated to achieve good workability. The designed mix proportions of the bond specimens are presented in Table 1. The bond specimens in this study were divided into several groups according to different influencing factors. The labels of the specimens consisted of letters and numbers. For example, in a specimen labeled C30R50F1D5, C30 represents the concrete strength grade, R50 represents 50% RCA replacement ratio, F1 represents 1.0% steel fiber volume fraction, and D5 represents an anchorage length of five times of the steel bar diameter. The mechanical properties of HRB400 steel bar are listed in Table2.



(a) (b) (c)

Fig. 1 The physical characteristics of materials: (a) NCA, (b) RCA, and (c) steel fiber.

Table 1 Mix proportion of SFRAC (kg/m^3)

Group	Water	Cement	NCA	RCA	Sand	SF	PS	AW

C30R50F1D5	166	302	540	540	884	78	3.02	19.06
C45R50F1D5	166	415	512	512	839	78	4.15	18.08
C60R50F1D5	166	553	479	479	783	78	5.53	16.89
C45R0F1D5	166	415	1024	0	839	78	4.15	0
C45R100F1D5	166	415	0	1024	839	78	4.15	36.16
C45R50F0D5	166	415	512	512	839	0	4.15	18.08
C45R50F15D5	166	415	512	512	839	117	4.15	18.08
C45R50F1D3	166	415	512	512	839	78	4.15	18.08
C45R50F1D7	166	415	512	512	839	78	4.15	18.08

Notes: SF represents steel fiber, AW means additional water, PS represents polycarboxylate superplasticizer.

Table 2 Mechanical properties of steel bar.

Category	d/mm	f_y/MPa	f_u/MPa	δ_{st}/%	E_s/MPa
HRB400	16	450	590	39.3	2.0×10^5

Notes: d is the diameter, f_y is the yield strength, f_u is the ultimate strength, δ_{st} is the elongation at fracture, and E_s is the elastic modulus of the steel bar

2.2. Specimen design

A total of 9 groups of specimens were fabricated to evaluate the bond behavior of steel bar embedded in SFRAC. Since there were three specimens in each group, totally 27 bond specimens were tested. The design parameters included the strength grade of the SFRAC, RCA replacement ratio, steel fiber volume fraction, and anchorage length (l_a). Each specimen was a 150 mm × 150 mm × 150 mm concrete cube with a 16 mm diameter steel bar. The unbonded segments of the bond specimens were constructed by placing a polyvinylchloride (PVC) pipe, which was 4 mm larger than the diameter of the steel bar. The steel bar was embedded in the middle of the cubic specimen with a 35mm-long rigid PVC pipe placed at the loading and free ends. A detailed schematic of the bond specimen used for the pullout test is shown in Fig. 2.

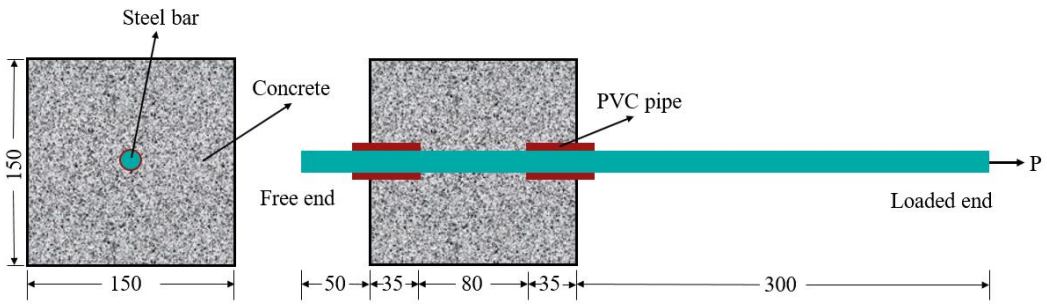


Fig. 2 Schematic of the pull-out specimen (units: mm).

2.3. Test setup and measurements

The pull-out tests were performed on a 1000 kN general electro-hydraulic servo testing machine produced by Jinan Sanqin Testing Technology Company, as illustrated in Fig. 3. The test frame consists of two thick steel plates with the holes at four corners linked together by four threaded bars. The upper steel plate was connected to the upper load cell of the testing machine through an auxiliary screw rod. The steel bar at the loading end of the bond specimen passed through the reserved hole in the bottom plate of the test frame and was clamped to the lower jaw of the testing machine. The loading rate was set to 0.3 mm/min and kept constant during the entire testing process until the slip of the free end exceeded 18 mm or a sharp decline in the load occurred. The loaded-end slip of the bond specimen was measured by a displacement meter installed on both sides of the loaded end of the steel bar, and the average value was taken as the loaded-end slip. In addition, to measure the slip at the loaded end caused by elongation of the steel bars and compression deformation of concrete, a displacement meter was mounted on the side of the specimen to measure its size. During the pullout test, the free end of the steel bar was in an unconstrained state; thus, the measured slip at the free end represented its relative slip value with SFRAC. All the test instruments were connected to a static strain testing system to automatically collect the test data during the loading process.

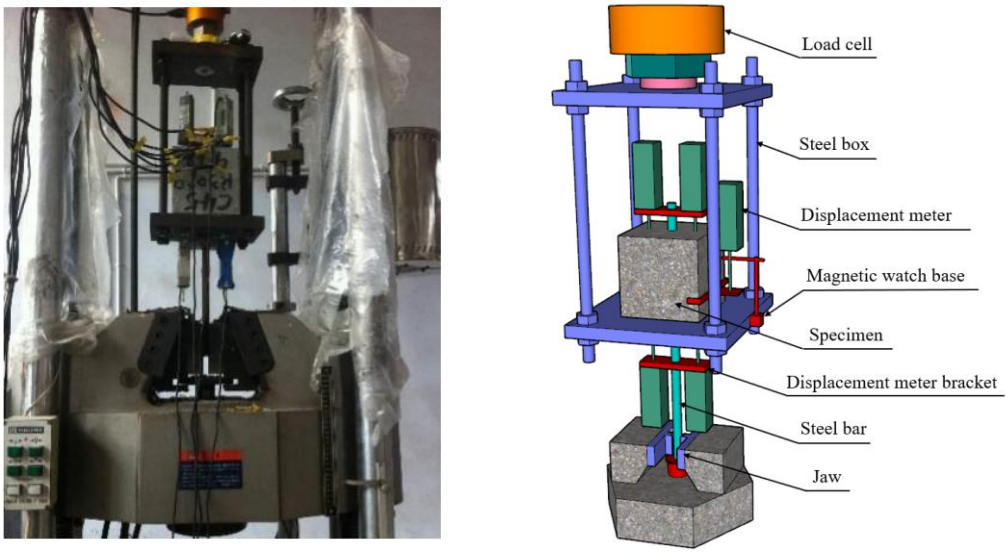


Fig. 3. Test setup of pull-out testing

In this study, the anchorage length was five times the steel bar diameter. If the anchorage length of the steel bar in concrete is short, it can be assumed that the bond stress of the steel bar in the bond segment is uniform, and the average bond stress in the bond part can be used to evaluate the bond characteristics. Thus, the nominal bond strength (τ) was assumed to be the uniform bond stress along the bond length at the load, which was obtained using Eq. (1):

$$\tau = \frac{P}{\pi \cdot d_s \cdot l_a} \tag{1}$$

where P is the maximum pullout load, d_s is the diameter of the steel bar and l_a is the embedded bar length. The experimental results for each specimen and mechanical properties of the SFRAC are listed in Table 3.

Table 3 Experimental results of bond specimens and mechanical properties of SFRAC.

Group	f_{cu}/MPa	f_{ts}/MPa	E_c/MPa	s_u/mm	τ_u/MPa	τ_r/MPa	Failure mode
C30R50F1D5	36.76	3.47	3.2×10^4	1.49	13.91	10.48	Pullout 3
C45R50F1D5	59.99	5.64	3.3×10^4	2.04	22.50	15.21	Pullout 3
C60R50F1D5	81.91	7.95	3.7×10^4	2.27	27.49	20.72	Pullout 1 Steel bar yield 2
C45R0F1D5	64.22	5.97	3.6×10^4	1.70	25.18	16.21	Pullout 3

C45R100F1D5	53.52	5.20	3.0×10^4	1.19	20.32	14.33	Pullout 3
C45R50F0D5	33.31	2.24	3.1×10^4	1.77	21.54	8.77	Splitting 3
C45R50F15D5	62.72	6.84	3.4×10^4	1.58	22.69	15.49	Pullout 3
C45R50F1D3	63.28	5.34	3.3×10^4	0.95	34.22	30.87	Pullout 3
C45R50F1D7	55.49	5.84	3.3×10^4	0.32	18.35	12.61	Steel bar yield 3

Notes: f_{cu}, f_{ts}, and E_c are the cube compressive strength, split tensile strength, and Young's modulus of concrete, respectively. τ_u and τ_r represent ultimate and residual bond strength, respectively. The number after the failure mode represents the number of damaged bond specimens.

3. Experimental results and discussions

3.1. Failure mode

Table 3 indicates the failure modes of the bond specimens, which are categorized into splitting, steel bar yield, and pullout failures, as shown in Fig. 4.

The splitting failure of the bond specimens mainly occurred in the concrete without steel fibers. At the beginning of the test, when the load was small, the relative slip between the steel bar and concrete mainly appeared at the loaded end, at which time the free end had not yet experienced apparent slip, and there were no obvious cracks in the bond specimens. With an increase in load, the loaded-end slip gradually propagated to the free end, and microcracks began to appear on the side of the bond specimen. When the load reached the ultimate value, the bond specimen suddenly cracked. Subsequently, the load decreased sharply, the slip at the free and loaded ends no longer increased, and the steel bar was completely separated from the concrete, causing the bond specimen to split into two to three pieces. At that time, the load immediately decreased to zero. Therefore, the failure mode of concrete splitting exhibited a brittleness characteristic. From the destruction surface of the bond specimens, it was observed that most of the RCA particles have broken from the middle, and the phenomenon of NCA fracture is slight. This may be because the relatively weak interface transition zone (ITZ) makes it easier for external forces to penetrate the RAC, resulting in the formation of cracks.

The steel bar yield failure mainly occurred in the bond specimens with a higher concrete grade, higher steel fiber content, and longer anchorage length. With an increase in load, the steel bar first yielded before the bond stress reached the maximum, and then the steel bar was pulled off. The concrete had no apparent cracks in this state, and the bond specimens still exhibited good integrity.

The pullout failure mainly occurred in the bond specimens with a high steel fiber content and small anchorage length. With an increase in load, the relative slip between the steel bar and concrete increased, and a small crack at the steel bar loaded end appeared through the surface of the bond specimen. As the load increased further, the steel bar slowly disengaged from the concrete, at which point the slip continued to increase, and the load decreased gradually. Owing to the crack resistance of the steel fibers, there were only tiny and concentrated cracks on the surface when the bond specimen was destroyed. At that moment, the integrity of the bond specimens was good and they still exhibited a certain bonding ductility.



(a) (b) (c)

Fig. 4. Failure modes: (a) splitting, (b) steel bar yield, and (c) pullout failures.

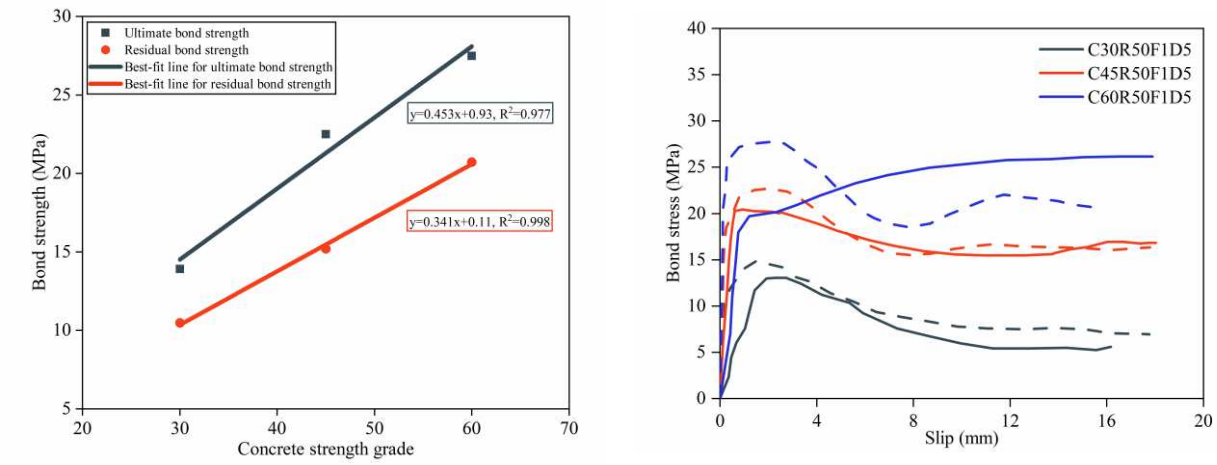
3.2. Bond behavior

3.2.1. Effect of concrete strength grade

Fig. 5(a) shows the effect of the concrete strength grade on the bond strength. It can be seen that the ultimate and residual bond strength increases with an increase in the concrete strength grade. In comparison with the bond specimen with concrete strength of C30, the ultimate bond strength of the SFRAC bond specimens with C45 and C60 strength grades are increased by 61.75% and 97.63%, respectively. The residual bond strengths are increased by 45.13% and 97.70%, respectively. This is because the higher the concrete strength grade, the higher the density and crack resistance. Therefore,

the occurrence of internal cracks in the bond specimens was delayed, and the chemical adhesion and mechanical interlocking forces of the steel bars increased, thereby further increasing the bond strength.

Fig. 5(b) displays the bond stress-slip curves between the steel bars and SFRAC with different strength grades. The free-end bond stress-slip curves clearly change with an increase in the concrete strength grade. In the ascending section, the slope and ultimate bond stress of the bond stress-slip curve increase with increasing concrete strength grade. In the descending section, the descending rate of the bond stress-slip curve increases with an increase in the concrete strength grade. In the residual section, the residual bond stress increases with increasing concrete strength grade. For the C60R50F1D5 bond specimen, an increase in the bond stress causes the tensile stress of the steel bars to exceed the yield strength, and the steel bars yield before reaching the ultimate bond stress. Therefore, the bond stress-loaded-end slip curve shows the tensile stress-displacement curve of the steel bars.



(a) (b)

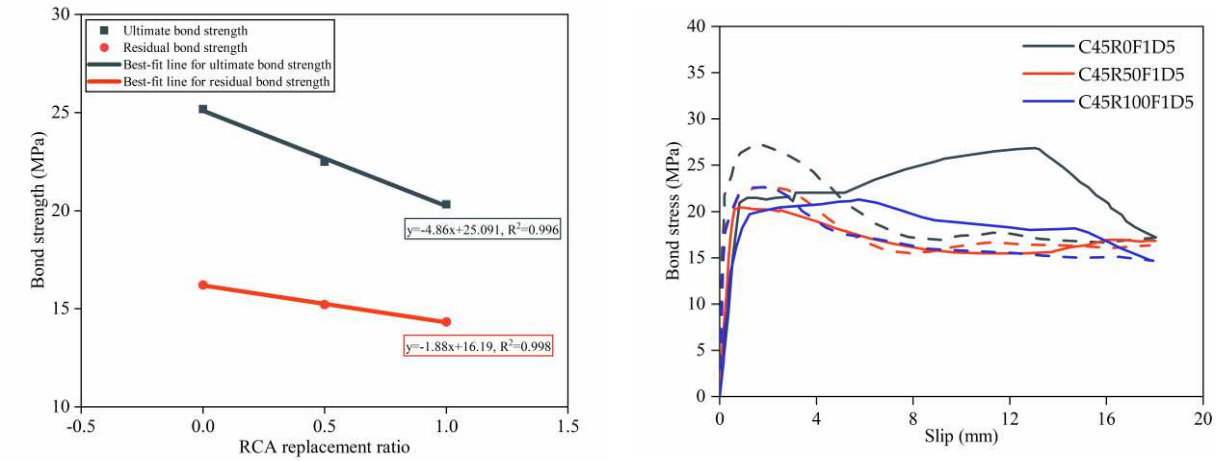
Fig. 5. (a) Bond strength and (b) loaded end (solid lines) and free end (dotted lines) bond stress-slip curves of bond specimens with different concrete strength grades.

3.2.2. Effect of RCA replacement ratio

Fig. 6(a) shows the effect of the RCA replacement ratio on the bond strength. It can be observed that the ultimate and residual bond strength decreases with an increase in the RCA replacement ratio. Compared to the specimen with RCA replacement ratio of 0%, the ultimate bond strength of specimens with RCA replacement ratios of 50% and 100% are decreased by 10.64% and 19.3%, respectively. The residual bond strength is decreased by 6.17% and 11.60%, respectively. This is mainly because the higher the RCA replacement ratio, the higher the content of low-strength RCA in the concrete.

Moreover, the area of the weak ITZ is larger, the ultimate and residual bond strength of the bond specimens are lower.

Fig. 6(b) depicts the bond stress-slip curves between the steel bars and SFRAC with different RCA replacement ratios. The shapes of the bond stress-slip curves at the free end are approximately the same. In addition, the larger the RCA replacement ratio, the lower the ultimate and residual bond stresses.



(a) (b)

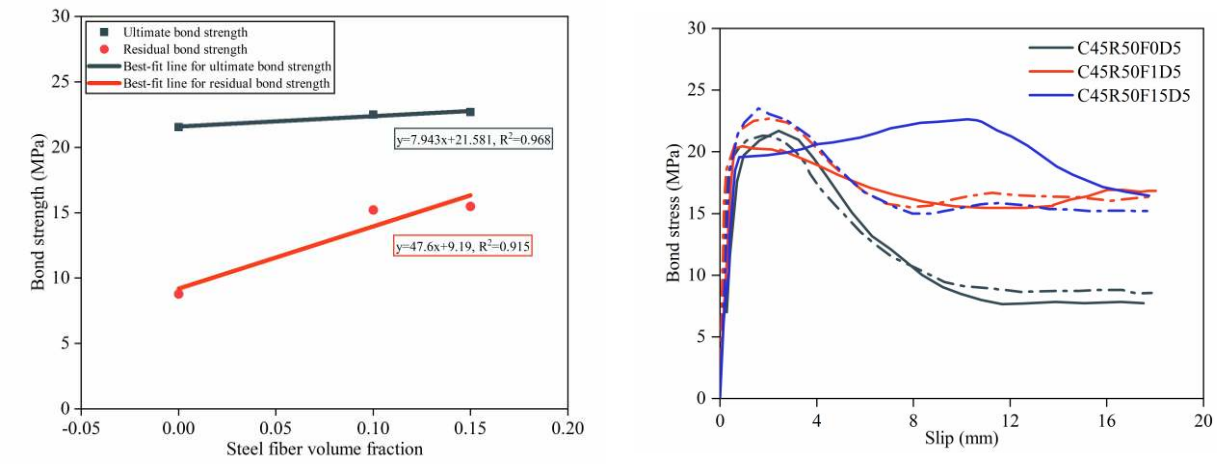
Fig. 6. (a) Bond strength and (b) loaded end (solid lines) and free end (dotted lines) bond stress-slip curves of bond specimens with different RCA replacement ratios.

3.2.3.Effect of steel fiber volume fraction

Fig. 7(a) shows the effect of the steel fiber volume fraction on the bond strength. It can be seen that the steel fiber volume fraction has little effect on the ultimate bond strength of the SFRAC bond specimens. It can be observed that the residual bond strength between the steel bars and SFRAC tends to increase with an increase in the steel fiber volume fraction. The residual bond strengths of the RAC bond specimens with steel fiber volume fractions of 1.0% and 1.5% increased by 73.43% and 76.62%, respectively, compared with those of the RAC bond specimens without steel fibers. Adding an appropriate amount of steel fibers can effectively hinder microcrack expansion in the concrete and delay the formation of macrocracks owing to the crack resisting and toughening effects of the steel fibers. For the RAC bond specimens, cracks are more likely to occur inside the matrix, which leads to a decrease in the concrete strength, and the increase in the bond stress tends to slow down. The addition of steel fibers changes the bonding inside the concrete matrix, making the aggregate and mortar more

closely connected and less prone to joint dislocation. In addition, the steel fibers occupy a part of the space, particularly the overlapping spatial effect of the steel fibers, which makes steel bars more tightly wrapped by the concrete.

Fig. 7(b) illustrates the bond stress-slip curves between the steel bars and SFRAC with different steel fiber volume fractions. The bond stresses of the ascending, descending, and residual sections of the bond stress-slip curves at the loaded and free ends tend to increase with an increase in the steel fiber volume fraction. For the C45R50F0D5 bond specimen, owing to the inherent brittleness of the RAC, the bond stress decreases rapidly after the peak state. For the C45R50F1D5 and C45R50F15D5 bond specimens, the mechanical anchoring effect of the steel fiber can provide the resistance to the bond slip when the bond specimen cracks, which delays the development of splitting cracks. Therefore, the residual bond stress increases with an increase in the steel fiber volume fraction.



(a) (b)

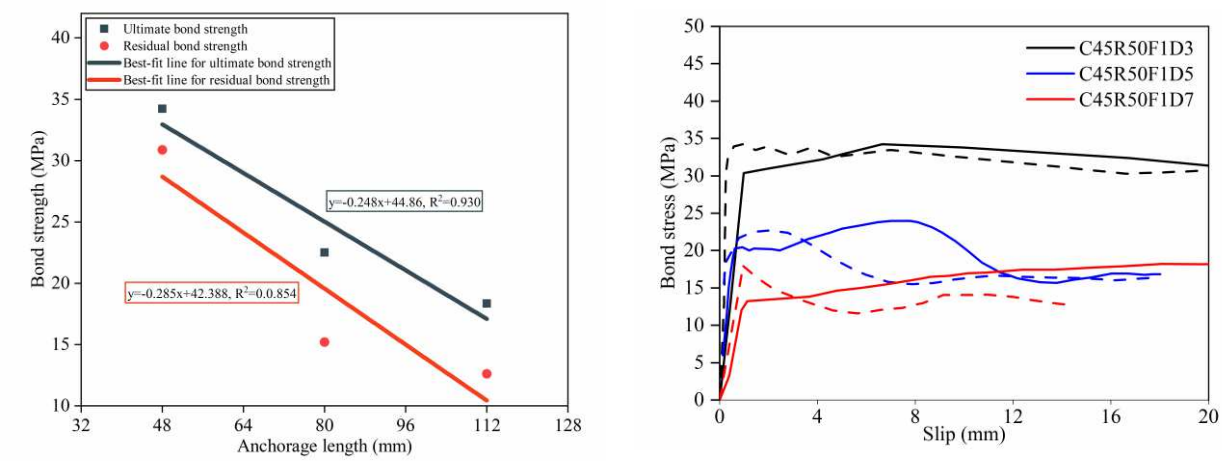
Fig. 7. (a) Bond strength and (b) loaded end (solid lines) and free end (dotted lines) bond stress-slip curves of bond specimens with different steel fiber volume fractions.

3.2.4. Effect of anchorage length

Fig. 8(a) shows the effect of the anchorage length on the bond strength. It can be seen that the ultimate and residual bond strength decreases with an increase in the anchorage length. Compared to the bond specimen with an anchorage length of 48 mm, the ultimate bond strengths of the SFRAC bond specimens with 80 mm and 112 mm anchorage lengths decreased by 34.25% and 46.38%, respectively, the residual bond strengths decreased by 50.73% and 59.15%, respectively. This is because the frictional resistance caused by the shrinkage of concrete and the mechanical interlocking

force caused by the uneven surface of the steel bar and concrete have a nonlinear distribution along the length of the steel bar. The closer to the loaded end, the greater the deformation, friction force, and mechanical interlocking force. In contrast, the part far away from the loaded end has less adhesive force. The larger the anchorage length, the more uneven the distribution of the bond stress on the surface of the steel bar after the specimen is stressed.

Fig. 8(b) depicts the bond stress-slip curves between the steel bars and SFRAC with various anchorage lengths. When the anchorage length ranges from 48 to 112 mm, the slope of the ascending section of the free end bond stress-slip curve gradually decreases; moreover, the increasing rate of the bond stress slows down, and the adhesive stress at the residual segment decreases. The residual stress is generated by the friction between the steel bar and surrounding concrete. The longer the anchorage length, the greater the residual stress because a long anchorage length increases the stress transmission path, resulting in a more significant friction force.



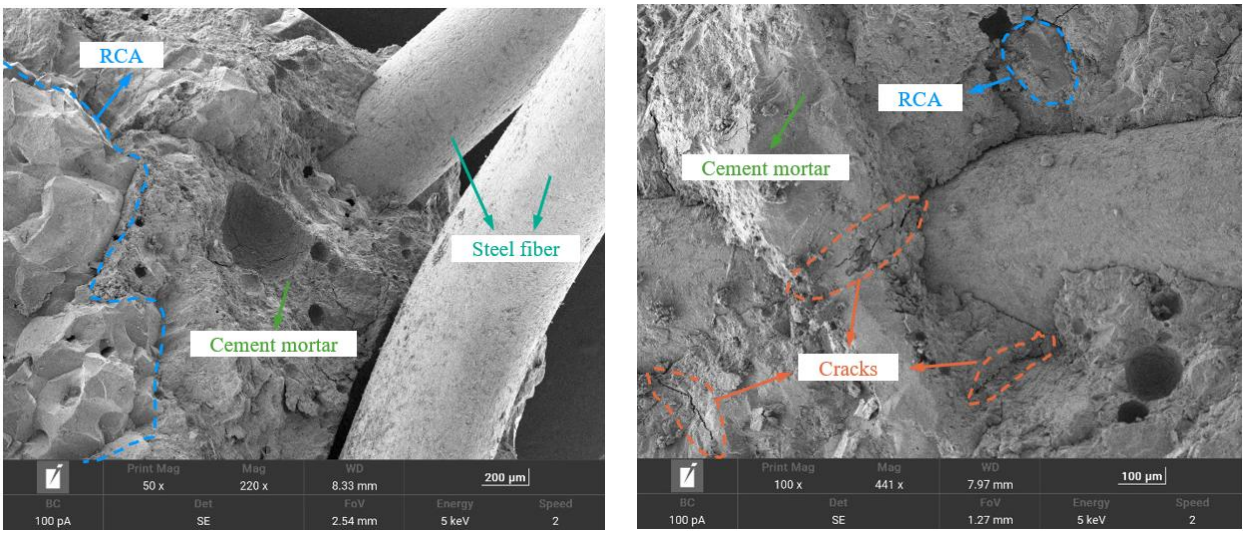
(a) (b)

Fig. 8. (a) Bond strength and (b) loaded end (solid lines) and free end (dotted lines) bond stress-slip curves of bond specimens with different anchorage lengths.

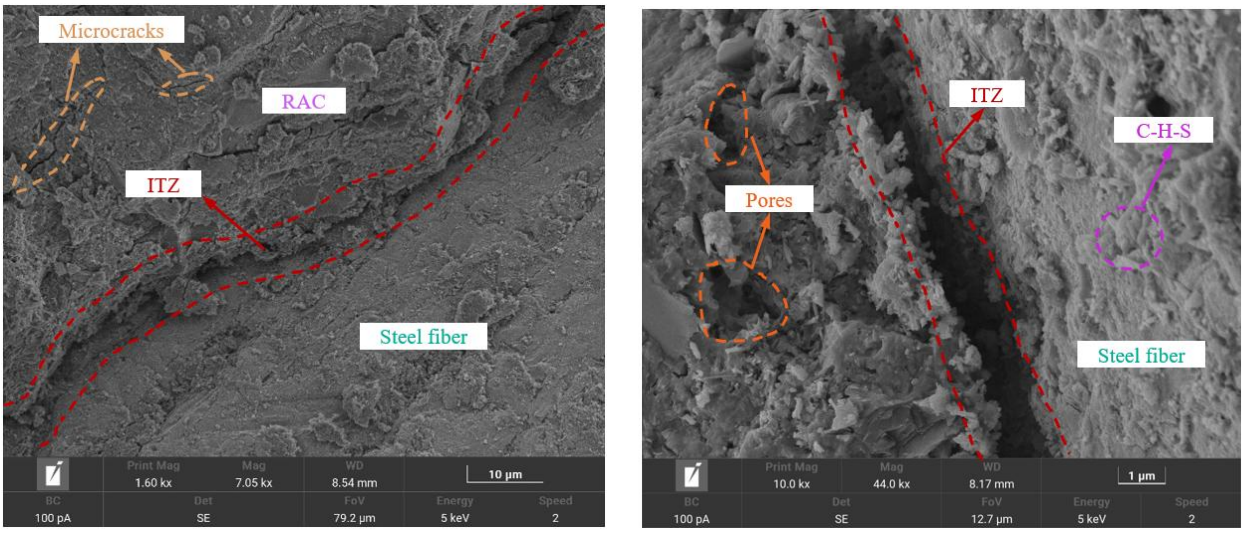
3.3. Mortar pores of SFRAC and microscopic morphology of the ITZ

The microstructural analysis of the SFRAC samples was performed using scanning electron microscopy (SEM). Fig. 9 displays the internal microstructure at different magnifications. Large steel fiber clusters formed voids and gaps at the interface between the steel bar and concrete matrix, which weakened the adhesion quality between them, as shown in Fig. 9(a). Fig. 9(b) shows the crack resisting effect of the ITZ near the steel fiber in the SFRAC. The steel fibers hinder the extension of wider

cracks and internal microcracks. Fig. 9(c) indicates that the steel fiber is firmly bonded to the cement base material. At the same time, the microcracks extend to the RCA, blocking the extension of microcracks and inhibiting their development into through–through cracks because the toughness of RCA is higher than that of the cement substrate. The ITZ between the steel fiber and cement mortar can be clearly distinguished in Fig. 9(d). Compared with the concrete matrix structure, the ITZ has a higher water-cement ratio, higher porosity, looser microstructure, and weaker area, which is destroyed first after being stressed. However, the surface of the steel fibers reacted with the $Ca(OH)_2$ generated by cement hydration to produce a large amount of C-S-H gel. Compared with the hydrated products of ordinary cement, SFRAC with appropriate steel fiber content has a higher strength.



(a) (b)



(c) (d)

Fig. 9. SEM image of SFRAC samples: (a) 50×, (b) 100×, (c) 1600×, and (d) 10000×.

3.4. Bond stress–slip constitutive model

To simulate the bond behavior of steel bars in the SFRAC bond specimens as accurately as possible, an analytical bond stress-slip constitutive model suitable for describing the bond behavior between steel bars and SFRAC was developed.

According to the measured results of the bond stress and slips at the free end of the steel bar in the bond section, the bond stress-slip relationship between the steel bars and SFRAC was simplified, as shown in Fig. 10, and expressed as follows:

Ascending section:

$$\tau = \tau_{\mathrm{fru}}\left(\frac{s}{s_{fru}^{l}}\right)^{\alpha_b},\ s \le s_{fru}^{l} \tag{2}$$

Horizontal section:

$$\tau = \tau_{fru},\ s_{fru}^{l} \le s \le s_{fru}^{r} \tag{3}$$

Descending section:

$$\tau = \tau_{frr} - \left(\tau_{frr} - \tau_{fru}\right)\frac{s_{frr}-s}{s_{frr}-s_{fru}^{r}},\ s_{fru}^{r} \le s \le s_{frr} \tag{4}$$

Residual section:

$$\tau = \tau_{frr}, s \ge s_{frr} \tag{5}$$

where τ_{fru} and τ_{frr} are the ultimate and residual bond stresses, respectively; τ_{fru}^{l} and τ_{fru}^{r} are the left and right boundary slips corresponding to the ultimate bond stress, respectively; and s_{frr} is the slip corresponding to the residual bond stress. To obtain the parameter α_b in Eq. 2, curve fitting was performed on the experimental data.

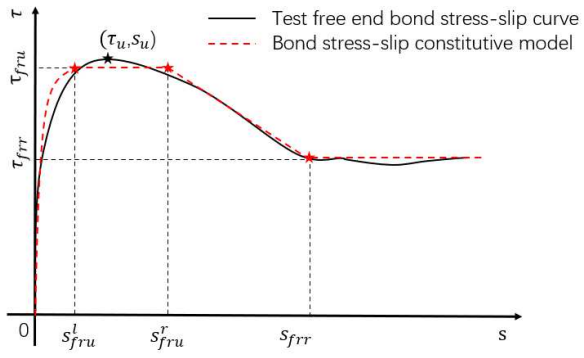


Fig. 10. Bond stress-slip curve.

Based on a comprehensive analysis of the measured bond stress-slip curve at the free end of the

bond specimen, the values of each characteristic parameter in Eq. (2)-(5) were obtained and listed in Table 4. It is worth noting that the characteristic parameter values of the bond stress-slip curve are related to the strength grade of SFRAC, RCA replacement ratio, steel fiber volume fraction, and anchorage length.

Table 4 Key parameter of bond stress–slip curves.

Group	s_{fru}^{l}	s_u	s_{fru}^{r}	τ_{fru}			τ_{frr}			α_b
	T	T	T	T	C	T/C	T	C	T/C	
C30R50F1D5	0.96	1.49	2.57	1	1	0.73	1	1	0.74	0.142
				3.47	8.43		0.48	4.17		
C45R50F1D5	1.02	2.04	2.77	2	2	0.92	1	1	0.83	0.142
				1.95	3.80		5.21	8.29		
C60R50F1D5	1.13	2.27	2.89	2	2	0.99	2	2	0.97	0.142
				7.39	7.65		0.72	1.26		
C45R0F1D5	0.91	1.7	2.23	2	2	1.00	1	1	1.00	0.121
				6.28	6.28		6.21	6.21		
C45R100F1D5	1.19	1.82	2.28	2	2	1.00	1	1	1.00	0.121
				1.57	1.57		4.33	4.33		
C45R50F0D5	1.09	1.77	2.66	2	1	1.22	8.77	8.77	1.00	0.148
				1.45	7.65					
C45R50F15D5	1.23	1.58	2.13	2	2	0.95	1	1	1.00	0.148
				2.93	4.19		5.49	5.49		
C45R50F1D3	0.85	0.95	2.21	3	3	1.07	3	2	1.12	0.142
				4.22	2.04		0.87	7.67		
C45R50F1D7	0.85	0.95	1.96	1	1	1.15	1	9.18	1.37	0.142
				7.96	5.63		2.61			
Average	1.02	1.61	2.41			1.00267			1.00389	
COV	0.13927	0.27487	0.13264			0.13856			0.17597	

Notes: T represents the test while C represents the calculate. COV denotes the coefficient of variation.

Through statistical analysis of the data in Table 4, the following were obtained:

$$\tau_{fru} = (5.697 - 0.528V_r + 0.206V_r^2 - 0.482\frac{l_a}{d})\sqrt{f_{cu}} \quad (6)$$

$$\tau_{frr} = (4.001 + 1.400V_r - 1.458V_c^2 + 2.996\lambda_f - 2.644\lambda_f^2 - 0.562\frac{l_a}{d})\sqrt{f_{cu}} \quad (7)$$

$$\lambda_f = V_f\frac{l_f}{d_f} \quad (8)$$

where V_r and V_f represent the RCA replacement ratio and steel fiber volume fraction, respectively;

and λ_f indicates the key parameter of the steel fiber. In addition, the measured value of s_{frr} is 8-10 mm, which was taken as the spacing of steel bar ribs 10 mm. s_{fru}^{l} was taken as 1.02 mm. s_{fru}^{r} was taken as 2.41 mm. α_b was taken as 0.142.

Combining this paper's test results and collecting the results of other relevant researchers, the predicted formulas for calculating the ultimate and residual bond strength were verified. The calculated values were compared with the experimental results, as shown in Fig. 11. The average value of the ratio of ultimate bond strength test value to calculated value is 1.013, and the coefficient of variation is 0.141. The average value of the ratio of residual bond strength test value to calculated value is 0.950, and the coefficient of variation is 0.208. It shows that the calculated values of ultimate and residual bond strength are in good agreement with the relevant test data. To sum up, the suggested formula can better predict the ultimate and residual bond strength between steel bars and SFRAC, and can be used for subsequent research on bond behavior.

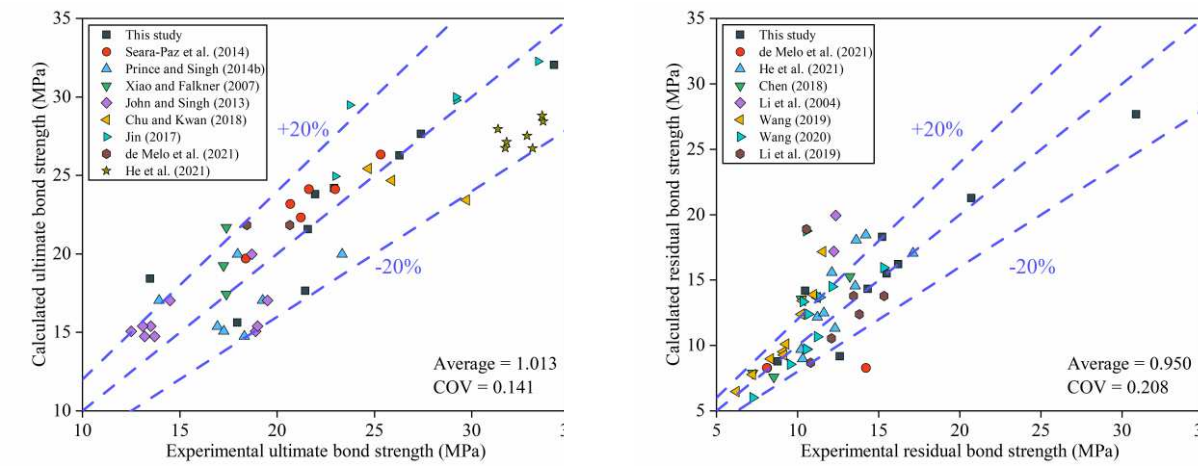


Fig. 11. Comparisons of calculated and experimental bond strength: (a) ultimate bond strength and (b) residual bond strength.

Fig. 12 shows a comparison between the experimental curves (solid lines) recorded during the pullout tests of bond specimens and calculated bond stress-slip constitutive curves (dotted lines). It can be observed that the bond stress-slip curves obtained from the constitutive model in this study are in good agreement with those of the experiments. Furthermore, the model can describe satisfactorily the global bond stress-slip response of the system for any parameter considered.

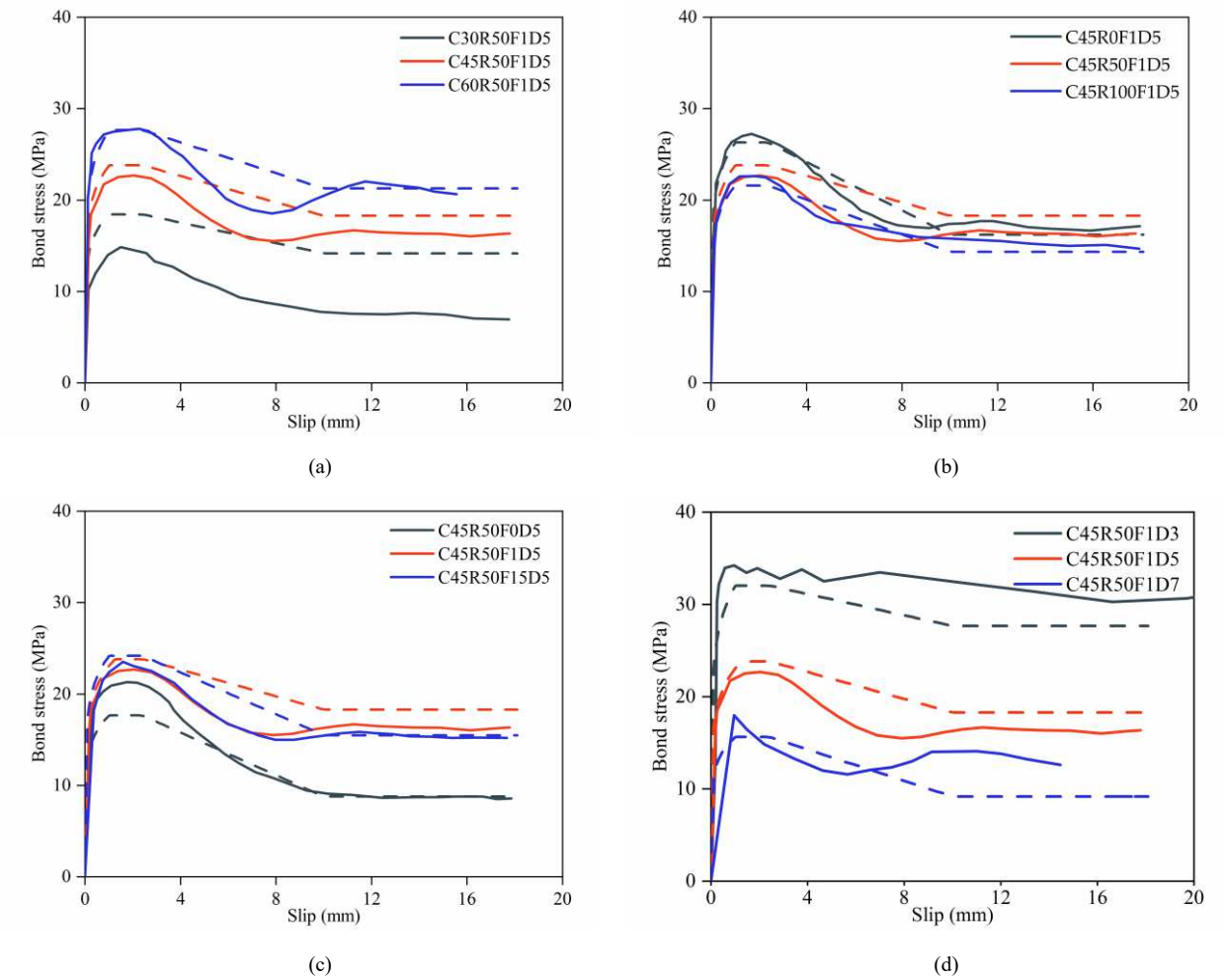


Fig. 12. Comparison between the bond stress-slip curves obtained from the calculated constitutive models (dotted lines) and from the experiments (solid lines): (a) concrete strength grade, (b) RCA replacement ratio, (c) steel fiber volume fraction, and (d) anchorage length.

4. Finite element model

4.1. Unit type selection and material properties

Numerical analyses of the pullout tests were performed using the ABAQUS finite element software. Given the geometry of the problem, a quarter-bond specimen model was adopted, in which the steel bar was positioned along the axis of symmetry, thus reducing the number of elements of the mesh.

In this study, a solid element was used to model the steel bars and concrete, and the three-dimensional solid element C3D8R with an eight-node reduced integral format was employed for both the steel bars and concrete elements. The existence of transverse ribs on the surface of the steel bar makes it difficult for the finite element calculation to converge. Thus, the surface of the steel bar

was smoothed and the biting force of the transverse ribs was considered by adjusting the parameters of the bonding unit. The spring2 double-spring coupling unit was selected to calculate the bonding effect between the steel bar and concrete. The bilinear isotropic elastic-plastic model built in the ABAQUS software was adopted. The plastic damage model was used for concrete, and the following parameters, namely, a concrete density of 2.35×10^{-9} t/mm^3, Poisson's ratio of 0.167, dilation angle of 30°, eccentricity of 0.1, ratio of initial equiaxial compressive yield stress to initial compressive stress (f_{b0}/f_{c0}) of 1.378, K_c value of 0.6667, and viscosity parameter of 0.05, were considered to execute the FEA model.

The uniaxial stress-strain relationship curve of the SFRAC under compression was defined by the following formula [47,48]:

$$y = \begin{cases} \dfrac{\xi x - x^2}{1 + (\xi - 2)x}, & 0 \le x \le 1 \\ \dfrac{x}{\psi(x-1)^2 + x}, & x > 1 \end{cases}$$

$$\xi = 3.92 + 0.7\lambda_f - 3.2V_r$$

$$\psi = 0.75 - 0.6\lambda_f + 0.78V_r$$

$$f_{cu} = f_{c,0}(0.825 - 0.144V_r)(0.633 + 0.633\lambda_f)$$

$$\varepsilon_c = (0.7 + 0.172\sqrt{f_c})(1 + 0.32\lambda_f)(1 + 0.22V_r)\cdot 10^{-3} \quad (9)$$

$$x = \frac{\varepsilon}{\varepsilon_c}$$

$$y = \frac{\sigma}{f_c}$$

$$f_c = 0.6f_{cu}$$

$$d_c = 1 - \sqrt{\frac{\sigma_t}{\varepsilon_t \cdot E_c}}$$

where ξ is a parameter related to the curvature of the ascending section, ψ is a parameter related to the curvature of the descending section, $f_{c,0}$ represents the concrete strength grade, ε_c is the critical strain corresponding to the ultimate stress of the SFRAC, ε is the nominal strain of the material obtained from the material property experiment, σ is the nominal stress of the material obtained from the material property experiment (in MPa), f_c is the prism compressive strength (in

MPa), ε_t is the true strain, σ_t is the true stress, and d_c is the uniaxial compression damage evolution parameter of the SFRAC.

The inelastic strain $\tilde{\varepsilon}$ was calculated according to Eq. (10):

$$\tilde{\varepsilon} = \varepsilon_t - \sigma_t / E_c \tag{10}$$

The uniaxial stress-strain relationship curve of the SFRAC under tension was defined according to the following formula:

$$\begin{gathered}
\alpha_t = 0.312 f_{ts}^2 \\
\varepsilon_{ts} = 65 f_{ts}^{0.54} \cdot 10^{-6} \\
\rho_t = \frac{f_{t,r}}{E_c \varepsilon_{ts}} \\
d_t = \begin{cases} 1 - \rho_t [1.2 - 0.2x^5], x \le 1 \\ 1 - \dfrac{\rho_t}{\alpha_t (x-1)^{1.7} + x}, x > 1 \end{cases} \\
\varepsilon = x \varepsilon_{ts} \\
\sigma = (1 - D_t) E_c \varepsilon \\
d_t = 1 - \sqrt{1 - D_t}
\end{gathered} \tag{11}$$

where ε_{ts} is the splitting tensile strain of the SFRAC (in MPa), d_t is the uniaxial tensile damage evolution parameter of the SFRAC, and D_t is the damage factor.

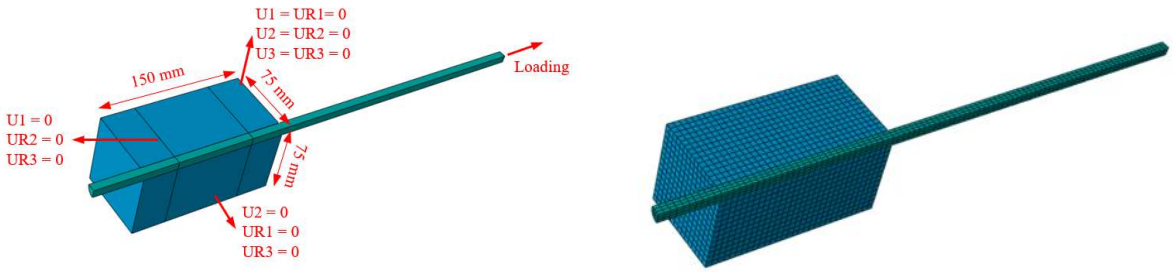
The cracking strain $\tilde{\varepsilon}_t$ was calculated using Eq. (12):

$$\tilde{\varepsilon}_t = \varepsilon_t - \sigma_t / E_c \tag{12}$$

4.2. Loading mode

Fig. 13 shows the generated geometry, applied loads, and boundary conditions for the finite element model of the steel bar pullout from the SFRAC. The specimen is symmetrical on the X and Y axes, so only the 1/4 structure of the experimental model was taken for analysis. The test block was constrained by the loading frame during the experiment, and it was regarded as a rigid body with six constrained degrees of freedom. Therefore, a fixed constraint was set to constrain its six degrees of freedom. The loading scheme of the ABAQUS finite element software provides two methods: displacement control and force control. This study adopted the displacement control method, which can easily converge and is realized by defining the displacement of the loaded end of the steel bar in the boundary conditions. A reference point at the steel bar loaded end was established, and the reference

point was coupled with the side surface of the steel bar loaded end. During the finite element analysis, a displacement-controlled load of 18 mm with a 0.3 mm/s loading speed was applied at the loaded end of the steel bar. The reason for imposing a displacement on the steel bar was to obtain a more gradual failure process compared to that of a similar loading scheme using applied force.



(a) (b)

Fig. 13. (a) Geometric model of bond specimen and (b) mesh model.

4.3. Modeling of contact elements

The contact surface with the SFRAC has normal and tangential functions. In the normal contact mode, contact is difficult, and the tangential nonlinear spring element spring2 was used to simulate the bond stress-slip behavior of the interface. Because only a linear spring can be defined in the pre-processing of the ABAQUS software, it is necessary to generate an INP file, and then modify the linear spring in the INP file into a nonlinear spring. In this study, first, two points were randomly selected to define linear spring A during pre-processing, and then the nonlinear spring (spring-2) was redefined by modifying the INP file. The nonlinear constitutive relation of the spring was defined by the curve of the force and displacement, in which the force was calculated using the following formula:

$$F = \tau \times A \tag{13}$$

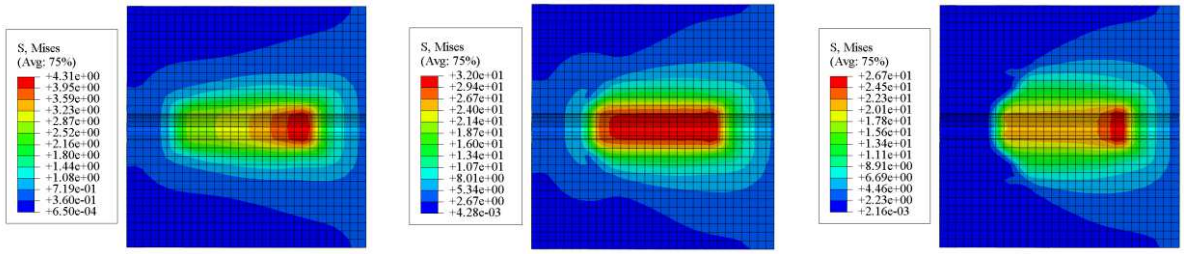
where A is the area occupied by the spring connection surface. The middle point is the sum of each quarter of the areas of four adjacent blocks, and the boundary point is the sum of each quarter of the areas of two adjacent blocks or one-quarter of the areas of one adjacent block. The bond stress τ was calculated using the bond stress-slip constitutive model in Section 3.3.

4.4. Verification of finite element model

4.4.1. Stress cloud

Fig. 14 depicts the stress cloud diagram for different values of slip for the concrete of the C45R50F1D5 bond specimen. As can be seen, at the beginning of the force application, the loaded end

of the steel bar is affected by more stress, which overcomes the chemical adhesion and frictional forces, gradually increasing the distribution of plastic strain along the steel bar. Finally, as shown in Fig. 14(c), the steel bar begins to separate from the concrete, and the bond stress of the steel bar decreases rapidly at the free end.



(a) (b) (c)

Fig. 14. Stress cloud diagram for different amounts of slip for the C45R50F1D5 bond specimen: (a) slip of 0.11 mm, (b) slip of 2.29 mm, and (c) slip of 11.40 mm.

Fig. 15 displays the stress cloud diagram of the steel bar of the C45R50F1D5 bond specimen when the load reaches the maximum value. The position of the initial point of the anchorage section of the steel bar (near the loading end) is the maximum stress, and the stress at the free end is very small. With the continuous loading of displacement, the equivalent stress of the steel bar spreads to the middle along the bonding length until the free end. The simulation results show that the equivalent stress of the steel bar in the range of the bond length exhibits a nonlinear distribution along the anchorage length. It gradually decreases from the loading end to the free end, which is in accordance with the distribution law of the steel bar stress, indicating that the simulation results are accurate.

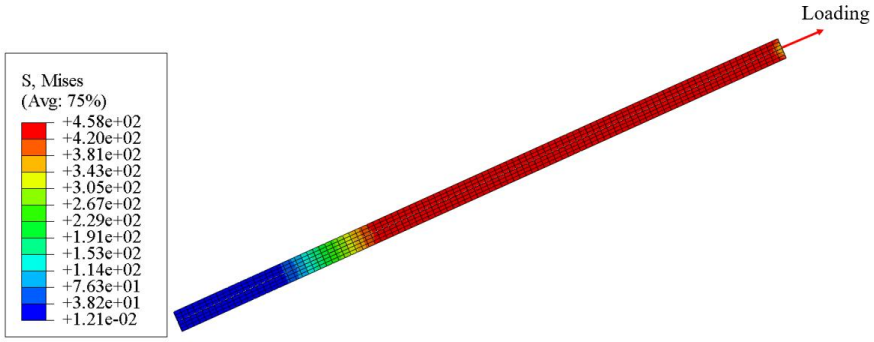


Fig. 15. Stress cloud diagram of the steel bar of the C45R50F1D5 bond specimen.

4.4.2. Load-slip curve at the loaded end

The load-slip curve of each specimen was obtained by simulation. As illustrated in Fig. 16, the

load-slip curves of all bond specimens are consistent with the overall change trend of the test curve, indicating that the model can accurately predict the peak load and the corresponding slip value of each specimen under different influencing factors. Furthermore, the shapes and change trends of the ascending and descending sections of the curve are relatively consistent.

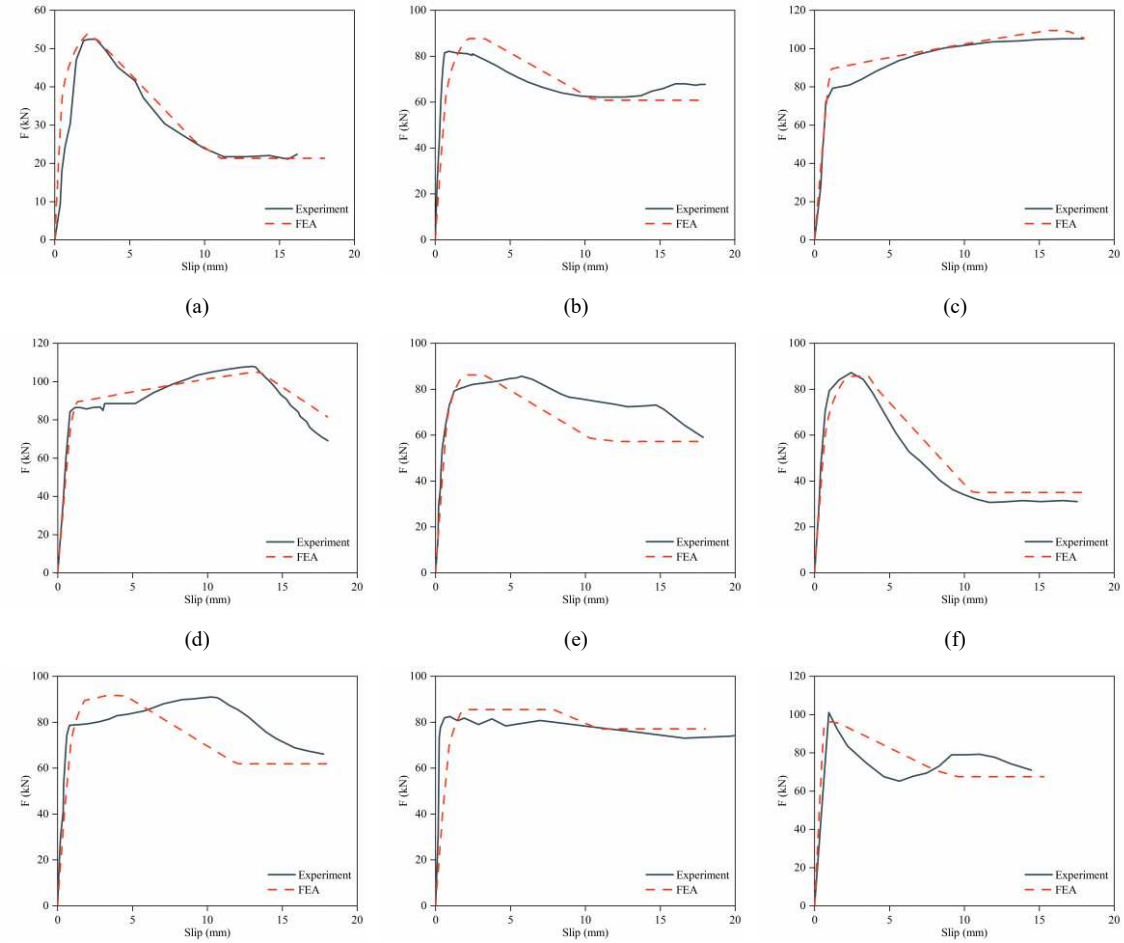


Fig. 16. Comparison of predicted and experimental load-slip curves: (a) C30R50F1D5, (b) C45R50F1D5, (c) C60R50F1D5, (d) C45R0F1D5, (e) C45R100F1D5, (f) C45R50F0D5, (g) C45R50F15D5, (h) C45R50F1D3, and (i) C45R50F1D7.

To summarize, the proposed constitutive model has good compatibility with the numerical model, and the numerical simulation has good precision and accuracy. In addition, the selection of the bonding unit and setting of the model parameters are reasonable and accurate. Furthermore, the simulation method of building nonlinear springs in batches is effective in verifying the pullout test, which can reasonably simulate the slip between the steel bars and SFRAC.

5. Conclusions

Based on the analysis of the experimental results in this study, main conclusions can be obtained as follows:

(1) The failure modes of the SFRAC bond specimens mainly include splitting, steel yield, and pullout failures. The ultimate and residual bond strength between the steel bars and SFRAC tends to increase with an increase in the concrete strength grade and decrease with an increase in the RCA replacement ratio and anchorage length. The addition of steel fiber has little effect on the ultimate bond strength of the SFRAC bond specimens, but it can greatly improve the residual bond strength. The SEM results revealed that the addition of steel fibers to the SFRAC bond specimens hinders crack propagation and reduces the crack propagation length.

(2) According to the bond stress-slip curve obtained from the test results and the calculation formula of ultimate and residual bond strength obtained from the analysis, the bond stress-slip curve between the steel bars and SFRAC was simplified into four parts, namely, ascending, horizontal, descending, and residual sections, and a four-section bond stress-slip constitutive model was developed. A comparison of the test results with the theoretical prediction results shows their similarity. Moreover, the developed theoretical model can better simulate the bond–slip performance between the steel bars and SFRAC.

(3) The spring element modeling method established in this study can conveniently and accurately complement ABAQUS in establishing the finite element model of the SFRAC structure considering the bond behavior, which greatly reduces the workload of researchers. The finite element method can accurately simulate the bond stress-slip relationship between the steel bars and SFRAC.

Funding declaration: This work was supported by the Henan Province Science and Technology Research Project (Grant no. 252102320299, no.262102320058).

References

[1] A. Akhtar, A.K. Sarmah. Construction and demolition waste generation and properties of recycled aggregate concrete: a global perspective, J. Clean. Prod. 186 (2018) 262-281,

445 https://doi.org/10.1016/j.jclepro.2018.03.085.
446 [2] B. Wang, L. Yan, Q. Fu, B. Kasal. A Comprehensive Review on Recycled Aggregate and
447 Recycled Aggregate Concrete. Resources, Conservation & Recycling 171 (2021) 105565,
448 https://doi.org/10.1016/j.resconrec.2021.105565.
449 [3] J. Xie, S. Kou, H. Ma, W. Long, Y. Wang. Advances on properties of fiber reinforced recycled
450 aggregate concrete: Experiments and models. Construction and Building Materials 277 (2021)
451 122345, https://doi.org/10.1016/j.conbuildmat.2021.122345.
452 [4] R. Silva, J. De Brito, R. Dhir. Establishing a relationship between modulus of elasticity and
453 compressive strength of recycled aggregate concrete, J. Clean. Prod. 112 (2016) 2171-2186,
454 http://dx.doi.org/10.1016/j.jclepro.2015.10.064.
455 [5] C. Thomas, J. Seti´en, J. Polanco, I. Lombillo, A. Cimentada. Fatigue limit of recycled aggregate
456 concrete. Construction and Building Materials 52 (2014) 146-154,
457 https://doi.org/10.1016/j.conbuildmat.2013.11.032.
458 [6] Guo H, Shi C, Guan X, Zhu J, Ding Y, Ling T-C, Zhang H, Wang Y. Durability of recycled
459 aggregate concrete-A review. Cem Concr Compos 89(2018)251-9.
460 [7] Breccolotti M, Materazzi AL. Structural reliability of bonding between steel rebars and recycled
461 aggregate concrete. Construction and Building Materials 47(2013) 927-934,
462 https://doi.org/10.1016/j.conbuildmat.2013.05.017.
463 [8] Kim S, Yun H. Influence of recycled coarse aggregates on the bond behavior of deformed bars in
464 concrete. Engineering Structures 48(2013) 133-143,
465 https://doi.org/10.1016/j.engstruct.2012.10.009.
466 [9] Behera M, Bhattacharyya SK, Minocha AK, Deoliya R, Maiti S. Recycled aggregate from C&D
467 waste & its use in concrete-A breakthrough towards sustainability in construction sector: A review.
468 Construction and Building Materials 68(2014) 501-16.
469 [10] M.J. McGinnis, M. Davis, A. de la Rosa, B.D. Weldon, Y.C. Kurama. Strength and stiffness of
470 concrete with recycled concrete aggregates. Constr. Build. Mater. 154 (2017) 258-269.
471 [11] K.P. Verian, W. Ashraf, Y. Cao. Properties of recycled concrete aggregate and their influence in
472 new concrete production. Resour. Conserv. Recycl. 133(2018) 30-49.

[12] Gao D, Zhang L, Nokken M. Compressive behavior of steel fiber reinforced recycled coarse aggregate concrete designed with equivalent cubic compressive strength. Construction and Building Materials 141(2017) 235-244, https://doi.org/10.1016/j.conbuildmat.2017.02.136.

[13] Wang C., Yuan J., Zhang Y., Ma Z.. Study on the mesoscopic mechanical behavior and damage constitutive model of micro-steel fiber reinforced recycled aggregate concrete, Construction and Building Materials 443 (2024) 137767, https://doi.org/10.1016/j.conbuildmat.2024.137767.

[14] Md. J. Islam, K. Islam, Md. Shahjalal, E. Khatun, S. Islam,A. B. Razzaque. Influence of different types of fibers on the mechanical properties of recycled waste aggregate concrete, Construction and Building Materials 337 (2022) 127577, https://doi.org/10.1016/j.conbuildmat.2022.127577.

[15] Xiao J, Falkner. Bond behaviour between recycled aggregate concrete and steel rebars. Construction and Building Materials 2007, 21(2):395-401, https://doi.org/10.1016/j.conbuildmat.2005.08.008

[16] Kim S, Yun H, Park W, Jang Y, Bond strength prediction for deformed steel rebar embedded in recycled coarse aggregate concrete. Materials & Design 83(2015)257-269, https://doi.org/10.1016/j.matdes.2015.06.008

[17] Cao W, Lin D, Qiao Q, Chen G, Jiang W, Peng S. Experimental study on bond-slip properties and influencing factors between rebars and recycled concrete. Journal of Natural Disasters 2017,26(5)

[18] C. Rockson, K. Tamanna, M. S. Alam, A. Rteil. Effect of rebar embedment length on the bond behavior of commercially produced recycled concrete using beam-end specimens, Construction and Building Materials 286 (2021) 122957, https://doi.org/10.1016/j.conbuildmat.2021.122957

[19] E.D. Reis, R.C. de Azevedo, A.L. Christoforo, F.S.J. Poggiali, A.C.S. Bezerra. Bonding of steel bars in concrete: A systematic review of the literature. Structures 49(2023) 508-519, https://doi.org/10.1016/j.istruc.2023.01.141

[20] Kim S, Yun H. Evaluation of the bond behavior of steel reinforcing bars in recycled fine aggregate concrete. Cement and Concrete Composites 46(2014) 8-18, https://doi.org/10.1016/j.cemconcomp.2013.10.013

[21] O. Leibovich, D. Z. Yankelevsky. Bond behavior in pull-out of a ribbed rebar from concrete with recycled concrete aggregates. Case Studies in Construction Materials 17 (2022) e01607,

https://doi.org/10.1016/j.cscm.2022.e01607

[22] Q. Huang, D. Wang. Experimental study on bond-slip between steel bar and recycled aggregate concrete. Adv. Mater. Res. 250-253 (2011) 1651-1656

[23] Z. Li, Z. Deng, H. Yang, H. Wang. Bond behavior between recycled aggregate concrete and deformed rebar after Freeze-thaw damage. Construction and Building Materials 250 (2020) 118805, https://doi.org/10.1016/j.conbuildmat.2020.118805

[24] H. Yang, Y. Huang, L. Lv. Bond behavior between recycled aggregate concrete and steel rebar subjected to biaxial lateral pressure. Structures 41 (2022) 139-146, https://doi.org/10.1016/j.istruc.2022.04.085

[25] L. Hou, H. Sun, G. Liu, T. Huang, D. Chen. Bond strength of deformed reinforcement embedded in steel fiber reinforced concrete: Influencing factors and prediction model. Construction and Building Materials 407 (2023) 133436, https://doi.org/10.1016/j.conbuildmat.2023.133436

[26] K. Wu, H. Zheng, J. Zhao, H. Li, J. Lin. Experimental study on interfacial bond behavior and analysis of bond stress of steel and steel fiber reinforced concrete composite structure. Structures 30 (2021) 156-165, https://doi.org/10.1016/j.istruc.2021.01.005

[27] Vitor Moreira de Alencar Monteiro, Daniel Carlos Taissum Cardoso, Flavio ´ de Andrade Silva, Barzin Mobasher. The influence of steel fibers on the bond slip behavior between rebars and concrete: Experimental and analytical investigation. Construction and Building Materials 411 (2024) 134357, https://doi.org/10.1016/j.conbuildmat.2023.134357

[28] Y. Chen, Q. He, X. Liang, Z. Chen, H. Li. Experimental investigation on mechanical properties of steel fiber reinforced recycled aggregate concrete under uniaxial cyclic compression. Construction and Building Materials 387 (2023) 131616, https://doi.org/10.1016/j.conbuildmat.2023.131616

[29] Feng J., Jia X., Dong X., Wang P., Xu B., Wang Z.. Cyclic compressive behavior of hook-end steel and macro-polypropylene hybrid fiber reinforced recycled aggregate concrete. Case Studies in Construction Materials 19 (2023) e02310, https://doi.org/10.1016/j.cscm.2023.e02310.

[30] Islam Md. J, Labiba U W, Chowdhury T F, Md. Shahjalal, Mustafy T, Tusher T H. Bond behavior of galvanized iron fiber reinforced concrete with recycled coarse aggregate and model prediction using machine learning. Results in Engineering 25 (2025) 104087.

[31] S. Guo, Y. Ding, X. Zhang, P. Xu, J Bao, C. Zou. Tensile properties of steel fiber reinforced recycled concrete under bending and uniaxial tensile tests. Journal of Building Engineering 96 (2024) 110467, https://doi.org/10.1016/j.jobe.2024.110467

[32] D. Gao, L. Zhang. Flexural performance and evaluation method of steel fiber reinforced recycled coarse aggregate concrete. Construction and Building Materials 159 (2018) 126-136, https://doi.org/10.1016/j.conbuildmat.2017.10.073

[33] Gao D, Luo F, Yan Y, Tang J, Yang L.. Experimental investigation on the flexural performance and damage process of steel fiber reinforced recycled coarse aggregate concrete. Structures 51 (2023) 1205-1218, https://doi.org/10.1016/j.istruc.2023.03.122.

[34] Gao D, Zhang L, Zhao J, You P.. Durability of steel fibre-reinforced recycled coarse aggregate concrete. Construction and Building Materials 232(2020) 117119, https://doi.org/10.1016/j.conbuildmat.2019.117119.

[35] M H El Ouni, S Ha Ali Shah, A Ali, S Muhammad, M S Mahmood, B Ali, R Marzouki, A Raza. Mechanical performance, water and chloride permeability of hybrid steel-polypropylene fiber-reinforced recycled aggregate concrete. Case Studies in Construction Materials 16 (2022) e00831, https://doi.org/10.1016/j.cscm.2021.e00831.

[36] Anurag, S.K. Singh. Impact of using recycled demolition waste as aggregates in steel fiber reinforced self-compacting concrete on its durability properties. Materials Today: Proceedings 48 (2022) 1666-1672, https://doi.org/10.1016/j.matpr.2021.09.530.

[37] P. Li, S. Li, Z. Liu, Y. Lu, F. Yang. Study on the biaxial mechanical behavior of steel fiber reinforced recycled aggregate concrete. Construction and Building Materials 428 (2024) 136372, https://doi.org/10.1016/j.conbuildmat.2024.136372

[38] Y. Chen, Xiangli Liu, Peihuan Ye, Wenhai Zhang, Yunpeng Ji. Mechanical properties of recycled aggregate concrete reinforced with steel fibers under triaxial loading. Journal of Building Engineering 92 (2024) 109541, https://doi.org/10.1016/j.jobe.2024.109541

[39] Ping Li, Zhenzhen Liu, Yiyan Lu, Chenlong Lin, Wentao Ma. Mechanical behavior of steel fiber reinforced recycled aggregate concrete under dynamic triaxial compression. Composite Structures 320 (2023) 117161, https://doi.org/10.1016/j.compstruct.2023.117161

[40] Z. Gu, J. Wang , D. Gao, J. Zhao. Effects of steel fibers on the flexural behavior of recycled concrete beam: Testing and analysis. Journal of Building Engineering 85 (2024) 108718, https://doi.org/10.1016/j.jobe.2024.108718

[41] M. Mathew, K. Girija, A.R. Sreedevi. Shear behaviour of reinforced concrete beams using treated recycled coarse aggregates and steel fibres. Materials Today: Proceedings, https://doi.org/10.1016/j.matpr.2023.04.086

[42] D. Gao, W. Li, Y. Pang, Y. Huang. Behavior analysis and strength prediction of steel fiber reinforced recycled aggregate concrete column under axial compression. Construction and Building Materials 290 (2021) 123278, https://doi.org/10.1016/j.conbuildmat.2021.123278

[43] Z. He,Y. Chen,Y. Ma, X. Zhang,Y. Jin, J. Song. The study on bond-slip constitutive model of steel-fiber high-strength recycled concrete. Structures 34 (2021) 2134–2150, https://doi.org/10.1016/j.istruc.2021.08.103

[44] D. Gao, H. Yan, D. Fang, L. Yang. Bond strength and prediction model for deformed bar embedded in hybrid fiber reinforced recycled aggregate concrete. Construction and Building Materials 265 (2020) 120337, https://doi.org/10.1016/j.conbuildmat.2020.120337

[45] General Administration of Quality Supervision, Inspection and Quarantine of the People's Republic of China, Standardization Management Committee of the People's Republic of China. GB175-2007 Common Portland Cement. Beijing: China Standards Press, 2007.

[46] General Administration of Quality Supervision, Inspection and Quarantine of the People's Republic of China, Standardization Management Committee of the People's Republic of China.GB25177-2010 Recycled coarse aggregate for concrete. Beijing: China Standards Press, 2010.

[47] Gao D, Wang F. Effects of recycled fine aggregate and steel fiber on compressive and splitting tensile properties of concrete. Journal of Building Engineering 2021 44:102631, DOI: https://doi.org/10.1016/j.jobe.2021.102631

[48] Gao D, Zhang L, Nokken M. Compressive behavior of steel fiber reinforced recycled coarse aggregate concrete designed with equivalent cubic compressive strength, Construction and Building Materials 141(2017) 235-244, https://doi.org/10.1016/j.conbuildmat.2017.02.136.